Report

Where Water is Oxidized to Dioxygen: Structure of the Photosynthetic Mn_4Ca Cluster

Junko Yano[1,2†], Jan Kern[3†], Kenneth Sauer[1,2], Matthew J. Latimer[4], Yulia Pushkar[1,2], Jacek Biesiadka[5], Bernhard Loll[5,6], Wolfram Saenger[5] Johannes Messinger[7*], Athina Zouni[3*], Vittal K. Yachandra[1*]

[1] Melvin Calvin Laboratory, Physical Biosciences Division, Lawrence Berkeley National Laboratory, Berkeley, CA 94720, USA

[2] Department of Chemistry, University of California, Berkeley, CA 94720, USA

[3] Max-Volmer-Laboratorium für Biophysikalische Chemie, Strasse des 17 Juni 135, Technische Universität, D-10623 Berlin, Germany

[4] Stanford Synchrotron Radiation Laboratory, 2575 Sand Hill Road, Menlo Park, CA 94305, USA

[5] Institut für Chemie und Biochemie/Kristallographie, Freie Universität, Takustrasse 6, D-14195 Berlin, Germany

[6] Present address: Max-Planck-Institut für Medizinische Forschung, Abteilung für Biomolekulare Mechanismen, Jahnstrasse 29, D-69120 Heidelberg, Germany

[7] Max-Planck-Institut für Bioanorganische Chemie, Stiftstrasse 34-36, D-45470 Mülheim an der Ruhr, Germany

[†] These authors contributed equally to this work

[*] To whom correspondence should be addressed

Abstract

Oxidation of water to dioxygen is catalyzed within photosystem II (PSII) by a Mn_4Ca cluster, the structure of which remains elusive. Polarized extended X-ray absorption fine structure (EXAFS) measurements on PSII single crystals constrain the Mn_4Ca cluster geometry to a set of three similar high-resolution structures. Combining polarized EXAFS and X-ray diffraction data, the cluster was placed within PSII taking into account the overall trend of the electron density of the metal site and the putative ligands. The structure of the cluster from the present study is unlike either the 3.0 or 3.5 Å resolution X-ray structures, and other previously proposed models.

Oxygen present at ~20% in Earth's atmosphere comes mostly from photosynthesis that occurs in cyanobacteria, green algae and higher plants (*1*). These organisms have within photosystem II (PSII) an oxygen-evolving complex (OEC), where the energy of sunlight is used to oxidize water to molecular oxygen. The heart of the OEC is a cluster of four Mn and one Ca (Mn_4Ca) connected by mono- and di-μ-oxo or hydroxo bridges. The specific protein environment and one chloride are also essential for the water splitting activity (*1*). During water oxidation the OEC cycles through five different oxidation states, known as S_i-states (i = 0 to 4), that couple the one-electron photochemistry of the PSII reaction center with the four-electron chemistry of water oxidation (*2*).

The structure of the Mn_4Ca cluster and its role in the mechanism of water oxidation have been investigated using spectroscopic methods (*1*), especially EPR/ENDOR (*3-9*), X-ray spectroscopy (*10*), and FTIR (*11*). In addition, the recent X-ray diffraction (XRD) studies of single crystals of PSII provide critical information about its structure at 3.8 to 3.0 Å resolution (*12-16*). However, even the highest resolution XRD data presently available is insufficient to accurately determine the position of Mn, Ca and the bridging and terminal ligands. This is reflected by the differences in the placement of the metal ions and putative ligands in the 3.0 (*16*) and 3.5 Å (*14*) structures. Furthermore, at the X-ray dose and temperature used in the XRD studies, the Mn_4Ca cluster geometry is disrupted, initiated by the rapid reduction of Mn(III) and Mn(IV) present in the dark stable S_1 state to Mn(II), as shown by Mn X-ray absorption near edge spectra (XANES) and EXAFS studies of PSII single crystals (*17*).

EXAFS experiments with PSII require a significantly lower X-ray dose than XRD measurements (*17*), and the onset of radiation damage can be precisely determined and controlled by monitoring the Mn K-edge position, thus allowing collection of data from the intact Mn_4Ca cluster of PSII. In addition, EXAFS provides metal-metal/ligand distances

with high accuracy (~0.02 Å) and a resolution of ~0.1 Å. Mn- and Ca-EXAFS studies of frozen solutions of PSII preparations have provided accurate distances and the numbers of Mn-Mn, Mn-Ca and Mn/Ca-ligand vectors in the Mn_4Ca cluster (*10, 18-21*) and have led to the development of several possible structural models for the Mn_4Ca cluster (Fig. S1).

For polarized EXAFS experiments on one-dimensionally oriented membranes or three-dimensionally oriented single-crystals, the EXAFS amplitude is orientation dependent and proportional to $\sim\cos^2\theta$, where θ is the angle between the **e**-field vector of the polarized X-ray beam and the absorber-backscatterer vector. Therefore, this technique provides important additional geometric information about the metal site in metalloprotein single crystals (*22, 23*). Here we show that polarized EXAFS can be used to provide structural models of the Mn_4Ca active site revealing details currently unresolvable by XRD. Combining information from polarized EXAFS and XRD (*16*) leads to the placement of these models within the PSII protein environment.

PSII crystals from *Thermosynechococcus elongatus* in the dark-stable S_1-state were oriented such that the X-ray **e**-field vector was parallel to the *a*-, *b*-, or *c*-axis of the crystal unit cell. The total photon dose on the sample was kept at a safe 1 x 10^7 photons/μm^2 on the basis of detailed radiation damage studies on single crystals of PSII (*17*). After the Mn XANES and EXAFS spectra were collected, the orientation of the crystal was determined *in situ* by collecting X-ray diffraction patterns (*24*).

Figure 1A (top) shows the polarized Mn K-edge XANES spectra of PSII single crystals with the X-ray ***e***-field vector parallel to each of the orthogonal crystal unit cell axes, *a*, *b*, and *c*. The spectra show unique features at each orientation both in the main K-edge (1s to 4p) and the pre-edge region (1s to 3d transitions, see inset). The orientation-dependent differences are more clearly seen in the second-derivative plots (Fig. 1A, bottom).

The Fourier transforms (FTs) of the polarized Mn EXAFS of PSII single crystals are shown in Fig. 1B. Peak I has contributions from bridging and terminal O or N atoms at 1.8 to 2.0 Å; Peak II results from di-μ-oxo bridged Mn-Mn interactions at 2.7 to 2.8 Å; and Peak III contains contributions from mono-μ-oxo bridged Mn-Mn and Mn-Ca interactions at 3.3 and 3.4 Å, respectively. The EXAFS spectra show a pronounced dependence on the crystal orientation, indicating that the Mn_4Ca cluster is highly asymmetric.

A test of whether the redox state and the structure of the Mn_4Ca cluster in the single crystals is equivalent to that in active oxygen-evolving PSII solution samples is to calculate isotropic solution spectra (powder spectra) from the oriented single-crystal spectra and compare these to experimental solution spectra. The comparison of XANES and EXAFS spectra in Figs. 2A and 2B (and the corresponding second derivatives in the case of XANES in Fig. 2A, bottom) show that they are indistinguishable within the remarkably low noise of these experimental data. This result confirms the dichroism of the EXAFS spectra, and shows that the cluster geometry is not disrupted by radiation damage. Therefore, the data of Fig. 1B form a reliable basis for the elucidation of the structure and orientation of the Mn_4Ca cluster within PSII.

Initially we used the polarized EXAFS data to test the Mn_4Ca structures proposed on the basis of XRD data (*14, 16*). The comparison of the experimental data (Fig. 1B) with the polarized EXAFS spectra calculated for the XRD models at 3.5 (*14*) and 3.0 Å (*16*) resolution are shown in Fig. S3. The disagreement is striking; it is most likely due to the limited resolution and X-ray damage to the Mn_4Ca cluster during XRD measurements (*17*).

In the next step, the polarized EXAFS data were used to evaluate and filter the large number of previously proposed and feasible models for the Mn_4Ca cluster (Fig. S1, Mn_4 motifs **a-r**), including topologically related structures (the motifs from the XRD structures are **c** (*16*) and **n** (*14*)). For this filtering process, the polarized EXAFS for the proposed structural models was calculated as follows (Fig. S4, (*24*)): 1) each model was placed into

one PSII monomer, 2) the coordinates for the companion monomer were determined using the local C_2 symmetry of the dimeric PSII complex, 3) the coordinates for the four symmetry related dimeric units within the $P2_12_12_1$ crystal unit cell were determined, and 4) the EXAFS spectrum was calculated for the PSII single-crystal with the **e**-vector of the X-ray beam parallel to each of the crystal unit cell axes, *a*, *b*, *c*, using FEFF8 (*25*). To determine the optimal orientation, each of the inserted clusters was rotated stepwise within the PSII monomer with respect to the three axes (x, y, z; for definition see Fig. 3, top right). For each orientation the EXAFS spectra were calculated and compared to the experimental results shown in Fig. 1B. This process was continued until the rotational space was mapped sufficiently to determine whether a specific model complies with the polarized EXAFS data (*24*). The focus in our comparison was predominantly on the contribution to the EXAFS from Fourier peaks II and III, which are from Mn-Mn and Mn-Ca interactions that mainly define the motif for the Mn_4Ca cluster. This process rules out unsatisfactory cluster geometries with a high degree of confidence.

Range-extended EXAFS results (*21*) show that three short Mn-Mn distances between 2.7 and 2.8 Å are present in the Mn_4Ca cluster. The presence of the 2.8 Å Mn-Mn vector is observed as a shift of FT peak II to a longer distance along the *a*-axis in the polarized EXAFS data (Fig. 1B). In addition to the 2.8 Å vector, two 2.7 Å vectors are required to reproduce the FT peak II intensity, mainly along the *b* and *c*-axes. (see also EXAFS fit parameters in Table S1). Therefore models (Fig. S1A, motifs **a-j**) containing only two short 2.7 Å, or one 2.7 Å and 2.8 Å Mn-Mn distances were unacceptable in reproducing both the solution range-extended EXAFS (*21*) and polarized EXAFS data.

The remaining models contain three Mn-Mn vectors at 2.7 to 2.8 Å (Fig. S1B, motifs **k-r**), and 0, 1, or 2 Mn-Mn vectors at 3.3 Å. Solution Mn EXAFS shows that FT peak III is best fit to one Mn-Mn vector at 3.3 Å and two Mn-Ca vectors at 3.4 Å (*10*), which is supported by Sr/Ca EXAFS results (*19, 20*). Models with these distances,

represented by motifs **p-r** in Fig. S1B, and models containing two 3.3 Å Mn-Mn distances (Fig. S1B, motifs **l-o**) along with the Mn-Ca distances were included in our search for a match with the observed dichroism (heterogeneity of ~0.2 Å was included for models with two 3.3 Å Mn-Mn vectors to decrease the otherwise too intense contribution to FT peak III).

Applying the rigorous testing protocol described above showed that the polarized EXAFS data (Fig. 1B) are consistent with three topologically related structures (Fig. 3, Model I, II and III) that are based on the Mn_4 motif **r** (Fig. 3, top) (*18, 21*). These models are shown in Fig. 3 in the orientation (indicated by the axis system shown in Fig. 3, top right) required to satisfy the polarized EXAFS data. The experimental polarized spectra (Fig. 1B) and the calculated spectra from the three structures positioned as shown (Fig. 3 left panel) are very similar, with regard to the intensity and the orientation dependence for FT peak II and III, which determine the motif of the structural model. The trend in the dichroism is also similar for FT peak I. Most of the contribution to peak I is from bridging O atoms, because terminal ligands are highly disordered (*10, 18*) (Table S1) and hence were not included in the simulations. The ambiguities in the intensities in FT peak I, however, come from the small contributions from this disordered shell of terminal ligands, which are difficult to model.

At present it is not possible to choose among the three models on the basis of the polarized EXAFS data. In addition, each of these structural models can have 16 symmetry equivalent orientations in the membrane (*24*). There are 8 orientations because of the four symmetry operations originating from the crystal space group $P2_12_12_1$ and the $\cos^2\theta$ dependence of the EXAFS signal and 8 more orientations from the non crystallographic C_2-symmetry of the monomers in the PSII dimer.

To further distinguish between these structural options we used the following

criteria: 1) the placement of Ca, 2) the distribution of the electron density from XRD (*16*), which is 'pear' shaped with the narrow end oriented towards the dimer C_2 axis, and 3) the information from the position of putative amino acid ligands identified around the electron density coinciding with the Mn_4Ca cluster (*16*). The placement of Ca relied on Sr EXAFS data showing that the two Mn-Sr(Ca) vectors are along the membrane normal (*20*), and the anomalous XRD studies indicating that Ca is above the 'Mn plane' towards the redox active tyrosine Y_Z and P_{680} chlorophylls (*14, 16*). The placement of Ca reduces by half the options among the symmetry related orientations. The remaining 8 symmetry equivalent orientations of Models I, II, and III were examined for compliance with the overall trend of the electron density and the placement of ligands (*24*). The best orientations of the three models within the PSII membrane are shown in Fig. 3. The other symmetry-related orientations are clearly unsatisfactory because of the pronounced asymmetry in the electron density.

The best fit to the ligand environment was obtained for Model II (coordinates in Table S2 (*24*)), while there was some overlap between the cluster and ligand positions with Model III (Fig. S5). The placement of Model I was even less satisfactory with regard to the ligands. The ligand assignments must remain tentative at this point, however, because movement of the protein ligand residues can result from radiation damage to the metal site during XRD (*17*). In the XRD study, the Mn close to Asp 170 (i.e. Mn_A) and Ca have a lower occupancy (σ value) compared to those of the other Mn atoms (*16*). This might indicate that they are more susceptible to radiation damage and hence their ligands may be prone to movement. If substantial ligand movements are considered, Models I and III cannot be excluded. The ligand environment for the best fit orientation for Model II is shown in Fig. 4

The considerable differences in the orientation and structures between Model II and those in the recent XRD proposals (*14, 16*) for the Mn_4Ca complex are shown as an overlay

in Fig. S6 (*24*). This highlights the difficulties of deriving high resolution structures from low resolution XRD. Although constraints from EXAFS distance information are included in the XRD model building which lead to approximate structures, there are too many structures that can be fit to the low resolution electron density. The importance of polarized EXAFS of single crystals lies in its ability to discriminate between the many possible high-resolution models by relying on the dichroism of the EXAFS spectra.

The structural changes of the Mn_4Ca complex on advancing through the S_i-state intermediates can be placed in the context of the polarized EXAFS data to assist in deriving a mechanism for photosynthetic water oxidation. The FTIR data, in conjunction with the best fit Model II (Fig. 4) suggests that Mn_A, which is ligated by Asp 170, does not change oxidation state and remains Mn(III) or Mn(IV) throughout the Kok cycle. The C-terminal Ala 344 may be a ligand to Mn_D, which is proposed to undergo Mn(III)->Mn(IV) oxidation during the S_1->S_2 transition (*26-28*). His 332 is likely to be a ligand of Mn_C. Recent FTIR data suggest that His 332 monitors structural changes of the Mn_4Ca cluster, but no evidence for a Mn-centered oxidation was reported (*29*). Accordingly Mn_C may remain Mn(III) or Mn(IV) throughout the cycle. Consequently, Mn_B is a likely candidate for Mn oxidation during the S_0->S_1 transition.

The dichroism in the polarized EXAFS data from single crystals provides a powerful filter for choosing among many proposed structural models. Also, as shown in this study, the combination of XRD and polarized EXAFS on single crystals has several advantages for unraveling structures of X-ray damage-prone, redox-active metal sites in proteins. XRD structures at medium resolution are sufficient to determine the overall shape and placement of the metal site within the ligand sphere, and refinement using polarized EXAFS can provide accurate metal-metal/ligand vectors. In addition, different intermediate states of the active site (including different metal oxidation states) can be studied, which may be difficult to study with XRD at high resolution. The structural model from polarized

EXAFS from the S_1-state presented here, and from the other S-states, will provide a reliable foundation for the investigation of the mechanism of photosynthetic water oxidation and for the design of biomimetic catalysts for water splitting.

References and Notes

1. T. Wydrzynski, S. Satoh (2005) *Photosystem II: The Light-Driven Water:Plastoquinone Oxidoreductase*, Springer, Dordrecht.
2. B. Kok, B. Forbush, M. McGloin, *Photochem. Photobiol.* **11**, 457 (1970).
3. T. G. Carrell, A. M. Tyryshkin, G. C. Dismukes, *J. Biol. Inorg. Chem.* **7**, 2 (2002).
4. G. W. Brudvig, *Adv. Chem. Ser.* **246**, 249 (1995).
5. K. Hasegawa, T.-A. Ono, Y. Inoue, M. Kusunoki, *Chem. Phys. Lett.* **300**, 9 (1999).
6. J. M. Peloquin, R. D. Britt, *Biochim. Biophys. Acta* **1503**, 96 (2001).
7. J. Messinger, J. H. A. Nugent, M. C. W. Evans, *Biochemistry* **36**, 11055 (1997).
8. K. A. Åhrling, S. Peterson, S. Styring, *Biochemistry* **37**, 8115 (1998).
9. L. V. Kulik, B. Epel, W. Lubitz, J. Messinger, *J. Am. Chem. Soc.* **127**, 2392 (2005).
10. V. K. Yachandra, K. Sauer, M. P. Klein, *Chem. Rev.* **96**, 2927 (1996).
11. H.-A. Chu, W. Hillier, N. A. Law, G. T. Babcock, *Biochim. Biophys. Acta* **1503**, 69 (2001).
12. A. Zouni*, et al.*, *Nature* **409**, 739 (2001).
13. N. Kamiya, J. R. Shen, *Proc. Natl. Acad. Sci. USA.* **100**, 98 (2003).
14. K. N. Ferreira, T. M. Iverson, K. Maghlaoui, J. Barber, S. Iwata, *Science* **303**, 1831 (2004).
15. J. Biesiadka, B. Loll, J. Kern, K. D. Irrgang, A. Zouni, *Phys. Chem. Chem. Phys.* **6**, 4733 (2004).
16. B. Loll, J. Kern, W. Saenger, A. Zouni, J. Biesiadka, *Nature* **438**, 1040 (2005).
17. J. Yano*, et al.*, *Proc. Natl. Acad. Sci. USA* **102**, 12047 (2005).
18. J. H. Robblee*, et al.*, *J. Am. Chem. Soc.* **124**, 7459 (2002).
19. R. M. Cinco*, et al.*, *Biochemistry* **41**, 12928 (2002).
20. R. M. Cinco*, et al.*, *Biochemistry* **43**, 13271 (2004).
21. J. Yano*, et al.*, *J. Am. Chem. Soc.* **127**, 14974 (2005).

22. R. A. Scott, J. E. Hahn, S. Doniach, H. C. Freeman, K. O. Hodgson, *J. Am. Chem. Soc*. **104**, 5364 (1982).

23. A. M. Flank, M. Weininger, L. E. Mortenson, S. P. Cramer, *J. Am. Chem. Soc*. **108**, 1049 (1986).

24. Materials and Methods are available as supporting material on *Science* online.

25. J. J. Rehr, R. C. Albers, *Rev. Mod. Phys*. **72**, 621 (2000).

26. H. A. Chu, W. Hillier, R. J. Debus, *Biochemistry* **43**, 3152 (2004).

27. R. J. Debus, M. A. Strickler, L. M. Walker, W. Hillier, *Biochemistry* **44**, 1367 (2005).

28. Y. Kimura, N. Mizusawa, T. Yamanari, A. Ishii, T. Ono, *J. Biol. Chem*. **280**, 2078 (2005).

29. Y. Kimura, N. Mizusawa, A. Ishii, T. Ono, *Biochemistry* **44**, 16072 (2005).

30. This work was supported by the Director, Office of Science, Basic Energy Sciences, Division of Chemical Sciences, Geosciences, and Biosciences of the Department of Energy (DOE) under Contract DE-AC02-05CH11231, by the NIH Grant (GM 55302), by the DFG (SFB 498, TP A4, C7 and Me 1629/2-3) and the Max-Planck-Gesellschaft. Synchrotron facilities were provided by SSRL operated by DOE, Office of Basic Energy Sciences. The SSRL Biomedical Technology Program is supported by NIH, NCRR, and by DOE, OBER. We thank Dr. Edward Berry (LBNL) for help with indexing the PSII XRD pattern and many insights, D. DiFiore and C. Lüneberg for technical assistance, and Drs. Uwe Bergmann (SSRL) and Pieter Glatzel (ESRF) for discussions about the analysis of polarization data. We are grateful to Profs. Mel Klein (1921-2000) and H.-T. Witt for their encouragement in initiating this collaborative research.

Supporting Online Material

www.sciencemag.org

Material and Methods

Figs. S1 to S6

Table S1 and S2

Figure Captions

Fig. 1

A. Single-crystal polarized Mn K-edge XANES spectra (top), and the corresponding second derivatives of the XANES spectra (bottom) of PSII in the S_1-state. The XANES spectra are shown with the X-ray **e**-field vector aligned parallel to the principal crystal axes (*a*, *b*, *c*) of PSII single crystals from *T. elongatus*: *a* (red), *b* (blue) and *c* (green). The inflection point of the edges and the shape of the spectra are clearly dependent on the orientation of the single-crystal with respect to the X-ray **e**-vector. The inset shows the dichroism of the pre-edge region assigned to the 1s to 3d transition.

B. Fourier transforms (FTs) of polarized Mn EXAFS spectra from single crystals of PSII in the S_1-state. The FTs are from EXAFS spectra with the X-ray **e**-field vector aligned parallel to the crystal unit cell axes of PSII: *a* (red), *b* (blue) and *c* (green). Each of the three FT peaks characteristic of Mn EXAFS from PSII is dichroic. FT peak I is from Mn-ligand backscattering, FT peak II is from three Mn-Mn distances at 2.7 - 2.8 Å, and FT peak III is from one Mn-Mn and two Mn-Ca distances at 3.3 and 3.4 Å respectively. The dichroism of the metal-metal distances reflects the geometry of the Mn_4Ca cluster.

Fig. 2

A. Comparison of Mn XANES spectra from solution PSII samples in the S_1-state (*T. elongatus*) (green) with the powder spectrum (red) calculated from the three PSII single-crystal polarized spectra (Fig. 1A). The corresponding second derivatives of the Mn XANES (bottom) reveal that the XANES spectra of the solution and calculated powder spectra from polarized PSII single crystal spectra are indistinguishable.

B. Comparison of the FTs of the Mn EXAFS spectrum from solution PSII samples (green) and the powder spectrum (red) calculated from the three PSII single-crystal polarized EXAFS spectra (Fig. 1B). The FTs are indistinguishable within the signal-to-noise ratio.

Fig. 3

High-resolution structural models for the Mn_4Ca cluster in PSII from polarized EXAFS. The Mn_4Ca Models I, II and III are shown on the right. Each is compatible with the polarized Mn EXAFS spectra of PSII single crystals. The common Mn_4 motif (**r** in Fig. S1) to the three structures is shown at upper left. The Models are shown in the orientation in which they should be placed in the PSII membrane according to the axis system shown at upper right. The *z*-axis is chosen to be along the membrane normal. The *x*-and *y*-axes define the membrane plane, the *x*-axis connects the two non-heme Fe atoms of the dimer that are related by the non-crystallographic local C_2-axis. The particular mirror images shown for Models I, II, III were chosen on the basis of their compatibility with the overall electron density and the positioning of the protein ligands in the 3.0 Å resolution X-ray crystal structure (*16*). The Mn atoms are shown in red. The distance between Mn_C and Mn_D atoms is ~2.8 Å (indicated by blue oxo bonds) and the distance between the Mn_A - Mn_B and Mn_B - Mn_C atoms is ~2.7 Å. The distance between Mn_B - Mn_D is ~3.3 Å. The Ca atom, shown in green, is at ~3.4 Å from two Mn atoms. The bridging motif to Ca is not well defined by our experiments; therefore, dashed lines connect the Ca to the two Mn atoms at ~3.4 Å. The experimental FTs from the polarized Mn EXAFS spectra from single-crystals (Fig. 1B) can be compared with the FTs calculated for these Models. The dichroism of the EXAFS spectra will be identical for several mirror images of the dimer in the PSII single-crystal (see text).

Fig. 4.

Placement of Model II for the Mn_4Ca cluster derived from polarized Mn EXAFS in relation to the putative ligands obtained from the 3.0 Å resolution X-ray crystal structure (*16*). The spheres represent Mn (red), Ca (green) and the bridging oxygen ligand atoms (gray). Terminal-ligand oxygen atoms from amino acid side chains are shown in orange. The

assignment of ligands is tentative because it is based on the electron density of the Mn_4Ca cluster, and its immediate environment that maybe altered by X-ray damage (see text). **A**. Stereo view of the electron density (*16*) with Model II placed in the density as explained in the text. The view is along the membrane plane. **B**. Same view as in **A**, ligands and atoms are labeled correspondingly. All ligands are from D1 except for CP43-Glu354. Electron density was omitted for clarity. **C**. A schematic of Model II with the view along the membrane plane, with putative ligands from the electron density. Bonds between Mn and bridging oxo are shown as solid green lines. Bonds to putative terminal ligand atoms from amino acids and to Ca are shown as dotted lines.

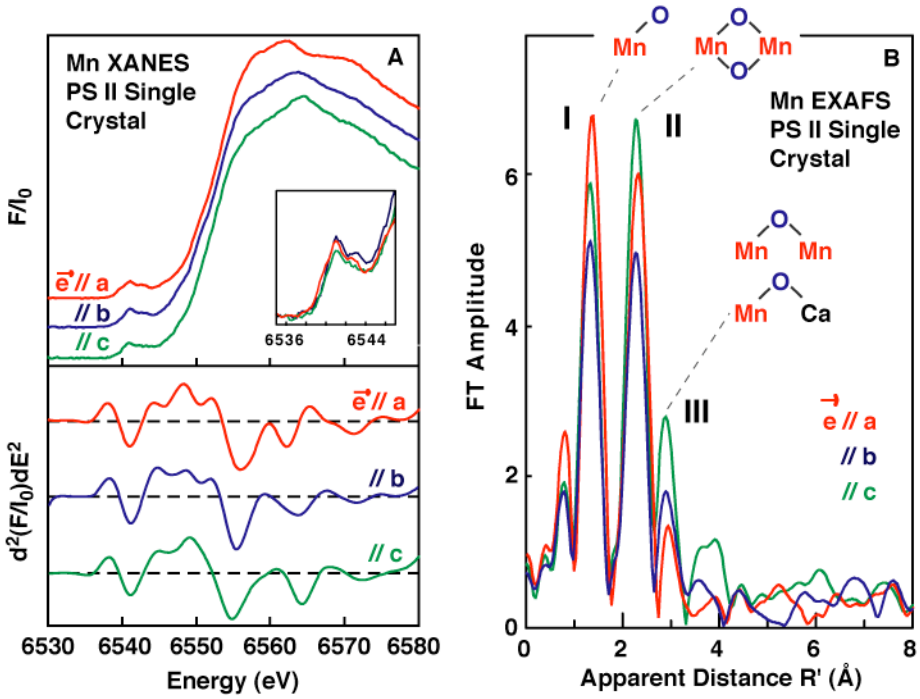
Mn XANES
PS II Single
Crystal
A
F/I0
e // a
// b
// c
6536
6544
d2(F/I0)dE2
e // a
// b
// c
6530 6540 6550 6560 6570 6580
Energy (eV)
Mn
Mn Mn
B
Mn EXAFS
PS II Single
Crystal
I
II
III
Mn Mn
Mn Ca
e // a
// b
// c
FT Amplitude
0 2 4 6
0 2 4 6 8
Apparent Distance R' (Å)

Fig. 1

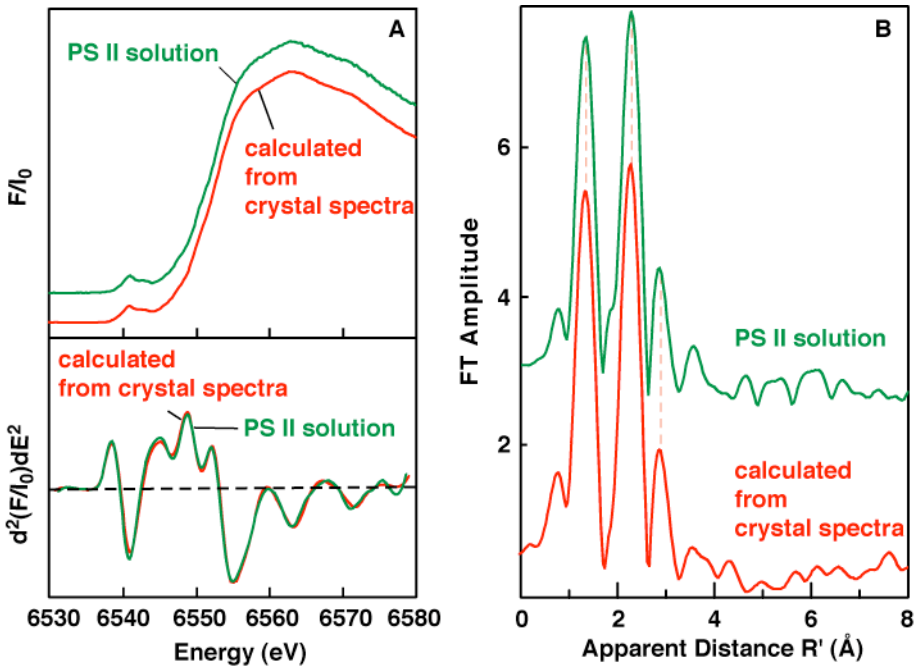
A
PS II solution
calculated
from
crystal spectra
F/I0
calculated
from crystal spectra
PS II solution
d2(F/I0)dE2
6530 6540 6550 6560 6570 6580
Energy (eV)
B
FT Amplitude
6
4
2
PS II solution
calculated
from
crystal spectra
0 2 4 6 8
Apparent Distance R' (Å)

Fig. 2

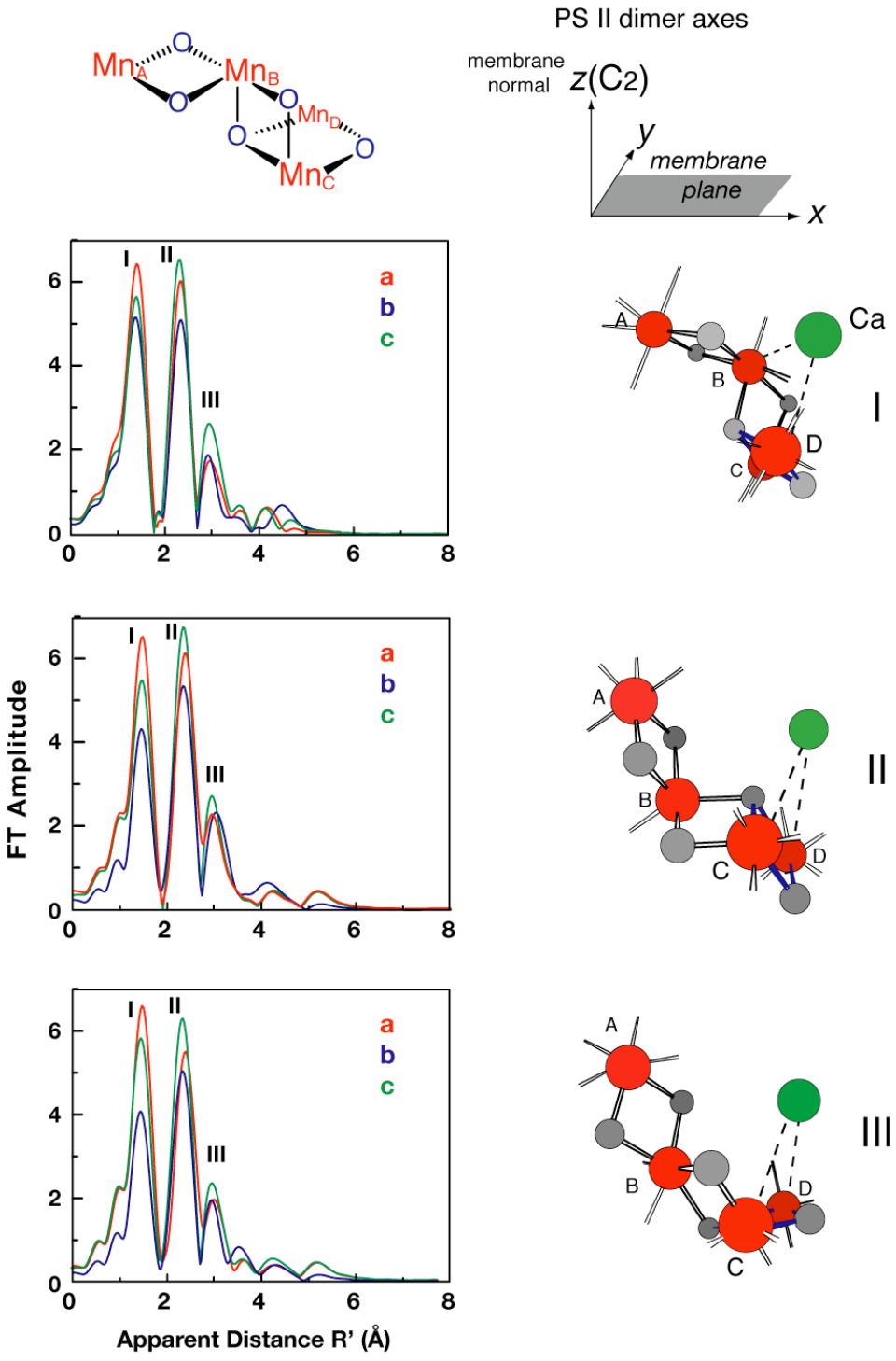
PS II dimer axes
membrane normal
z(C2)
y
membrane plane
x
Mn_A
Mn_B
Mn_D
Mn_C
O
I
II
III
a
b
c
FT Amplitude
Apparent Distance R' (Å)
Ca
A
B
C
D

Fig. 3

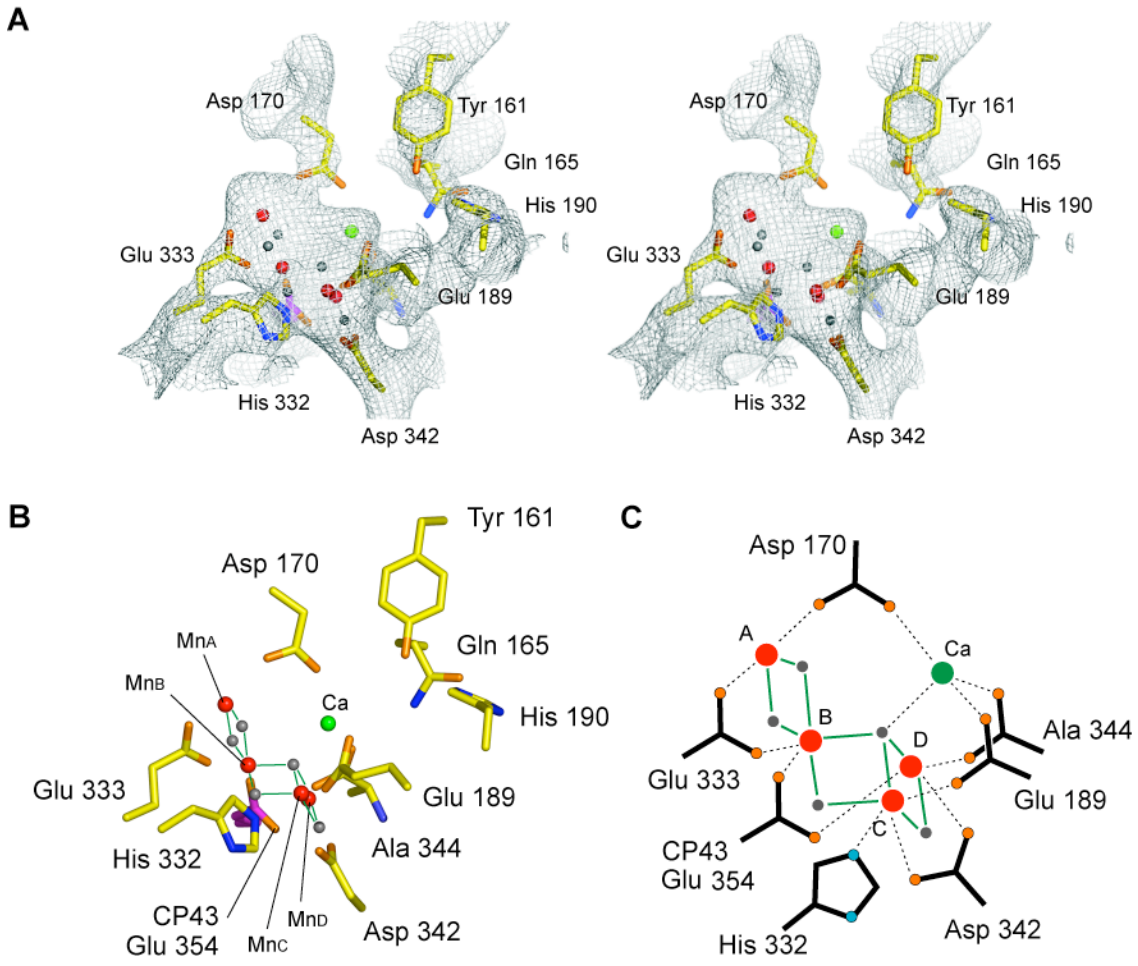
A
Asp 170
Tyr 161
Gln 165
His 190
Glu 333
Glu 189
His 332
Asp 342
Asp 170
Tyr 161
Gln 165
His 190
Glu 333
Glu 189
His 332
Asp 342
B
Tyr 161
Asp 170
MnA
Gln 165
MnB
Ca
His 190
Glu 333
Glu 189
Ala 344
His 332
CP43
Glu 354
MnC
MnD
Asp 342
C
Asp 170
A
Ca
B
D
Ala 344
Glu 333
Glu 189
C
CP43
Glu 354
His 332
Asp 342

Fig. 4

Supporting Online Material

Materials and Methods.

PSII crystals from *Thermosynechococcus elongatus* were prepared as described by Kern *et al*. (*S1*). PSII from *T. elongatus* crystallizes as a homodimer (the two monomers are related by a non-crystallographic local C_2 axis) in the orthorhombic space group $P2_12_12_1$ with four symmetry related dimers per unit cell. The PSII solution samples were prepared by dissolving crystals in a buffer containing ~50% glycerol, 50 mM PIPES-NaOH, pH 7.0, 3 mM $CaCl_2$, 0.015% n-dodecyl-β-D-maltoside at a PSII concentration of ~5 mM chlorophyll *a*.

The PSII crystals and solution samples were dark-adapted for one hour prior to freezing them in liquid N_2, to prepare them in the S_1-state. The samples were kept frozen until they were transferred to a liquid He cryostat at 9 ± 1 K for data collection. Control solution samples were illuminated at 200 K, and the multiline EPR spectrum from the S_2-state and the spectrum from the dark-adapted S_1-state were recorded to check for the quality of the samples and for the absence of any adventitious Mn(II). The PSII crystals chosen for XAS studies were from the same preparations that were used for XRD studies. Approximately 75 crystals were screened and data from 30 crystals (10 per orientation) with the best S/N ratios and orientation were used for the XAS analysis. The best S/N was obtained from larger crystals.

X-ray Absorption Spectroscopy (XAS) and X-ray Diffraction (XRD) Measurements. XAS spectra were obtained using a set-up specially designed for sequentially collecting the X-ray fluorescence and the X-ray diffraction (XRD) pattern from the same single crystal of PSII *in situ* without sample movement. This setup is shown in Fig. S2. The samples were kept at 9 ± 1 K in a He atmosphere at ambient pressure using an

Oxford CF-1208 continuous-flow liquid He cryostat.

X-ray absorption spectra were collected at the Stanford Synchrotron Radiation Laboratory (SSRL) on beamline 9-3 at an electron energy of 3.0 GeV and an average current of 70-100 mA. The intensity of the incident X-rays was monitored by a N_2-filled ion chamber (I_0) in front of the sample. The radiation was monochromatized by a Si(220) double-crystal monochromator which was detuned at 6600 eV to at least 50% of maximal flux to attenuate the X-ray 2nd harmonic. To decrease the sample damage by radiation, the incident X-ray beam was defocused at the sample position. The total photon flux on the sample was limited to 1 x 10^7 photons per μm^2, which was determined to be non-damaging on the basis of detailed radiation damage studies of PSII crystals and solution samples (*S2*). The samples were protected from the beam during spectrometer movements between different energy positions by a shutter synchronized with the scan program. Data were recorded as fluorescence excitation spectra using a germanium 30-element energy-resolving detector (Canberra Electronics). Energy was calibrated by the pre-edge peak of $KMnO_4$ (6543.3 eV), which was placed between two N_2-filled ionization chambers (I_1 and I_2) after the sample.

PSII solution samples were filled in home-built Plexiglas/Mylar-tape holders (40μl) and frozen. Six separate regions from one sample were used for the EXAFS scans and 4 scans were collected at each region. In total, 24 scans per sample were averaged for the EXAFS spectra.

Single crystals were mounted on home-built sample holders allowing the crystal to be oriented with the **e**-vector of the incident X-ray beam parallel to one of the principal axes of the crystal by using the crystal morphology as a guide. In this manner, the crystals were mounted with an accuracy of ± 10 degrees on average. Spectra were taken at only one orientation per crystal. To prevent damage prior to collection of XAS spectra, we measured

the X-ray absorption spectra first, followed by collection of the diffraction pattern to determine the more precise orientation of the crystal.

Eight XAS scans (20 minutes per scan) were collected per crystal, and the Mn K-edge was carefully monitored to verify that there was negligible damage to the Mn cluster. Only scans that showed negligible reduction of Mn as judged by the Mn K-edge were included in the summation. The X-ray dose used (1 x 10^7 photons per μm^2) corresponded to ~4 XAS scans of ~20 minutes.

A combination of XANES and EXAFS spectra was collected from 6400 to 7100 eV, 3eV/point from 6400-6535 eV, 0.2 eV/point from 6535 to 6576 eV, and 0.05 $Å^{-1}$/point in *k*-space from 2.07 to 12.0 $Å^{-1}$ (6576 eV to 7100 eV). In the *k*-space region, collection time was weighted using a cubic function from a minimum of 1 sec per point at low *k* values to a maximum of 20 sec per point at high *k* values. The XANES spectra were normalized to the post-edge EXAFS background. The XANES and EXAFS analysis was performed following methods described in detail previously (*S5, S6*).

X-ray diffraction patterns were collected for each crystal at two crystal orientations using a Mar345 image plate detector (MAR USA Inc.). Data were collected at the same orientation as the XAS measurement and then with the crystal rotated by 45 degrees from that orientation so as to improve the precision of the orientation determination. The exact orientation of each crystal used for the XAS measurement was determined by DENZO (*S3*) and MOSFLM (*S4*) on the basis of the two diffraction patterns. The orientation of each crystal with respect to the laboratory axes (defined as the direction of the X-ray **e**-field vector and the direction of propagation of the X-ray beam) was determined from the X-ray diffraction patterns obtained from the two orientations. Then the projection of each crystal axis (*a*, *b*, *c*) (i.e. direction cosines) on the X-ray **e**-vector was calculated. Only data from crystals with orientation less than ± 10 degrees on average away from any one of the

principal crystal axes were used for further analysis as described below. (1) For the data from such crystals, the spectral components from the two minor contributions (the components along 2nd and the 3rd axes) were subtracted, using the polarized spectrum from crystals that were close to perfect along the *a*, *b*, or *c*-axis. (2) The spectra of ~10 crystals per orientation were averaged to obtain the final data sets along the *a*, *b*, and *c* axes. In a 2nd cycle, the results of the first cycle were used for the corrections, and steps (1) and (2) were repeated for final refinement. The differences that resulted between the first and second cycles were minor and within the uncertainty of the polarized EXAFS method.

Polarized EXAFS Calculations and Comparison to Structural Models. Polarized and isotropic EXAFS spectra were calculated using *ab initio*-calculated phases and amplitudes from the program FEFF8 from the University of Washington (*S7, S8*). We developed a computer program that used coordinates from the Mn_4Ca model structures, placed them in the PSII crystal unit cell at the appropriate positions of the eight sites (four PSII dimers/unit cell), and input them to the FEFF8 protocol that could calculate the EXAFS spectrum and the FT along each of the *a*, *b* and *c*-axes of the crystal. The details are as follows (Fig. S4): (Step 1) Model structures such as those shown in Fig.S1 (first without Ca for the peak II dichroism, then with Ca for the entire dichroism) were inserted into the position of the Mn_4Ca cluster in the PSII monomer I. (Step 2) The monomer II coordinates were created from the monomer I using the local C_2 symmetry operation for the dimeric PSII. (Step 3) The dimer PSII was placed into the four symmetry related units within the orthorhombic $P2_12_12_1$ crystal unit cell. (Step 4) The EXAFS spectra of the PSII single-crystal with the **e**-vector of the X-ray beam parallel to each crystal axis, *a*, *b*, *c* were simulated using FEFF8. The inserted cluster at Step 1 was then rotated stepwise (10-20° steps at first, then 5° steps for more precise analysis) within each PSII monomer along each of the three axes (x, y, z; for definition see Fig. 3, top right), followed by steps 2, 3 and 4

described above to calculate the EXAFS spectra and the Fourier transforms. The increments in rotation angles were decreased in the vicinity of promising orientations. The FEFF8 calculations were performed with Debye-Waller parameters typical of those that have been used for PSII samples and multinuclear Mn complexes (*S5, S6*). To investigate the effect of multiple-scattering contributions, most of the calculations were carried out using 2, 4 and 8 legs of interactions. The final comparison between the calculated polarized EXAFS from the structural models with the experimental polarized EXAFS data from crystals was done using the 2-leg simulation data**.**

Comparison of Solution and Crystal EXAFS. Traditional EXAFS fits were also performed on solution and crystal EXAFS data, and the results were compared. These fits were used to show that similar EXAFS parameters could be used to fit data from both the solution and crystal data. The fit parameters for peak II or peaks II+III from PSII solution samples and crystals are shown in Table S1. The fits show that there are two short Mn-Mn vectors at ~2.7 Å and one longer Mn-Mn vector at 2.8 Å, and the fits from polarized EXAFS data are in good agreement with the solution data. It is significant that the intensity, as reflected by the N_{app} value in the fits of the Mn-Mn 2.8 Å vector for the crystal data, is predominantly along the *a* and *b* axes, with reduced intensity along the *c* axis. The fits also show that the longer Mn-Mn and Mn-Ca distances and the numbers of these vectors at distances of 3.3 and 3.4 Å from the single crystals are also in good agreement with the data from PSII solution samples.

Comparison of Structural Models from Single-Crystal EXAFS with Electron Density from XRD. From each of the models derived from the single crystal EXAFS results (Fig. 3), we generated the symmetry-equivalent orientations by taking account of the C_2-symmetry relating the monomers in the dimer, the four symmetry operations originating from the crystal space group $P2_12_12_1$, and all possible mirror images

on the crystallographic *ab*, *bc* or *ac* planes (owing to the $\cos^2\theta$ dependence of the EXAFS signal). This led to 16 different orientations of each model (8 from each monomer), all giving the same EXAFS dichroism.

For each symmetry-equivalent orientation of the Model I, II or III, the center of mass was translated to the center of electron density attributed to the Mn_4Ca cluster in monomer I in the XRD structure (*S9*), and rmsd (root mean squared deviation) between Mn atoms of the EXAFS model and the XRD model was calculated. The structures with the lowest rmsd were selected for further evaluation.

Among the symmetry equivalents of three structural models from single-crystal polarized EXAFS, Models II and III in the particular orientation shown in Fig. 3 fit extremely well to the PS II ligand environment and the overall trend of the electron density. The rmsd is 0.7 Å for Model II, 0.79 Å for Model III and 0.99 Å for Model I.

Model II in the ligand environment is shown in Fig. 4, and Model III in Fig. S5. However, it should be noted that the PSII electron density from XRD contains effects due to radiation damage (*S2, S9*). Therefore there could be some movement of the amino acid ligands induced by radiation damage to the Mn_4Ca cluster.

Supporting Text.

Comparison of Structures from Polarized EXAFS of Single-Crystals and XRD. The most significant differences between models from polarized EXAFS of single crystals and the recent XRD based models (*S9, S10*) for the structure of the Mn_4Ca complex are: 1) the Mn_A-Mn_B distance is 2.7 Å in the S_1 state and the Mn are connected by a di-μ-oxo bridge, rather than a mono μ-oxo (*S9*) or μ_4-oxo bridging O atom (*S10*). 2) There is only one 3.3 Å Mn-Mn distance and it is between Mn_B and Mn_D, not two such distances as proposed in *S9* and *S10,* 3) Our models contain only two ~3.4 Å Mn-Ca

distances, whereas there are three such interactions in both *S9* and *S10*. 4) The 2.8 Å Mn-Mn distance recently described in high-resolution EXAFS experiments (*S11*) is localized between Mn_C and Mn_D. The relative orientation of the 2.7, 2.8 and 3.3 Å Mn-Mn and 3.4 Å Mn-Ca vectors in our model are different from those in either *S9* or *S10*. Overlays of the models are shown in Fig. S6. The coordinates to Model II in the context of the 3.0 Å XRD structure (*S9*) is shown Table S2.

Supplementary Figures.

Fig. S1

Structural models (**a**-**r**) of the Mn cluster containing two or three short 2.7 to 2.8 Å Mn-Mn distances characterized by di-μ-oxo bridges and zero, one or two 3.3 Å Mn-Mn distances characterized by mono-μ-oxo bridges. The numbers in parentheses denote the number of short (2.7 to 2.8 Å) and long Mn-Mn (~3.3 Å) distances, respectively.

A. Topologically unique structures (**a**-**j**) with motifs that have been proposed containing (2,1), and (2,2) vectors are shown.

B. Topologically unique structures (**k**-**r**) with motifs that have been proposed containing (3.0), (3,1), and (3,2) vectors are shown. As noted in the text, three short (2.7 to 2.8 Å) and one long (3.3 Å) Mn-Mn distances are required to satisfy the solution and single-crystal EXAFS. Motifs (**p**-**r**) satisfy these criteria. Of these motifs only one option (**r**), has the requisite numbers of short and long Mn-Mn distances with the correct relative orientation to satisfy the dichroism observed in the single-crystal polarized EXAFS spectra. The topologically equivalent motifs to those proposed from X-ray crystallographic analyses are **c** (*S9*) and **n** (*S10*).

Fig. S2

The experimental set-up used for single-crystal X-ray absorption experiments. The PSII crystal was placed in a liquid He cryostat at a temperature of 9 ± 1 K at ambient pressure. The Mn XANES or EXAFS spectrum was measured as a fluorescence excitation spectrum using a 30-element energy-discriminating solid-state Ge detector placed at 90° to the incident beam. Downstream of the X-ray beam and the PSII crystal is the MAR 345 image plate detector that was used for obtaining the diffraction pattern from which the orientation matrix of the PSII crystal was determined by indexing the reflections. The incident X-ray beam is defined by the slits in the left foreground, and the I_0 ion chamber which is behind

the slits is used to measure the intensity of the incident beam. A shutter that protects the sample from damage during spectrometer motion is behind the ion chamber and before the cryostat.

Fig. S3

Comparison of the experimental Mn EXAFS dichroism from single-crystals of PSII with the polarized spectrum calculated from the proposed structures from XRD studies. The differences between the experimental spectra shown in the bottom panel and those calculated from the XRD coordinates for the Mn_4Ca cluster at 3.5 Å resolution (top panel, *S10*) and 3.0 Å resolution (middle panel, *S9*) are striking. The intensity and the dichroism pattern of FT peaks I, II and III (3.5 Å structure) and of FT peaks II and III (3.0 Å structure) are significantly different from the experimental data (bottom panel). The structure at 3.5 Å resolution specified coordinates for Mn, Ca and bridging ligand O and terminal ligand atoms. Therefore, all three Fourier peaks seen in the experimental data are present in the calculated spectra. For the 3.0 Å resolution structure Mn and Ca atoms and coordinated atoms of ligating amino acids were identified, but not the μ-oxo bridges because they were not resolved in the electron density. Hence, only FT peaks II and III, with contributions from Mn and/or Ca, are shown.

Note: To check whether the motifs in the 3.0 and 3.5 Å resolution structures (motifs **c** and **n** in Fig. S1) could generate the observed dichroism in an orientation different from the one that was proposed, the models were rotated about the PSII dimer axis system (as described in Fig. S4 and in the supplementary text) and the corresponding FTs along the *a*, *b* and *c* axis were compared to the experimental data. A match with the experimental data could not be obtained for these models in any orientation.

Fig. S4

Diagrammatic representation of polarized EXAFS simulation protocol describing the four

steps used for testing the viability of models for the Mn_4Ca cluster. The details are described in the main text and the supplementary material.

Fig. S5

Placement of Model III for the Mn_4Ca cluster derived from polarized Mn EXAFS in relation to the putative ligands obtained from the 3.0 Å resolution X-ray crystal structure (*S9*). The spheres represent Mn (red), Ca (green) and the bridging oxygen ligand atoms (gray). Terminal-ligand oxygen atoms from amino acids are shown in orange. The assignment of ligands is tentative because it is based on the electron density of the Mn_4Ca cluster, and its immediate environment that maybe altered by X-ray damage (see text). The view is along the membrane plane. All ligands are from D1 except for CP43-Glu354. Electron density was omitted for clarity.

Fig. S6

Comparison of Model II for the Mn_4Ca cluster derived from polarized Mn EXAFS with the models derived from the X-ray crystal structures at 3.0 Å (*S9*) and 3.5 Å (*S10*) resolution. The spheres represent Mn (red), Ca (green) and the bridging oxygen ligand atoms (gray) for Model II from polarized EXAFS of single crystals, and Mn (violet), Ca (cyan) and the bridging oxygen ligand atoms (yellow) for the X-ray crystal structures. Each overlay was generated using the best fitting position of Model II to the electron density (see Fig. 4) **A**. Overlay of Model II with the 3.0 Å resolution structure for the Mn_4Ca cluster (*S9*); protein ligands are omitted for clarity. The view is along the membrane plane. **B**. Same overlay as in **A**, but view is onto the membrane plane from the cytoplasmic (stromal) side. **C**. Comparison of Model II with the 3.5 Å resolution X-ray structure for the Mn_4Ca cluster (*S10*), protein ligands are omitted for clarity. The view is along the membrane plane. **D**. Same overlay as in **C**, but view is onto the membrane plane from the cytoplasmic side.

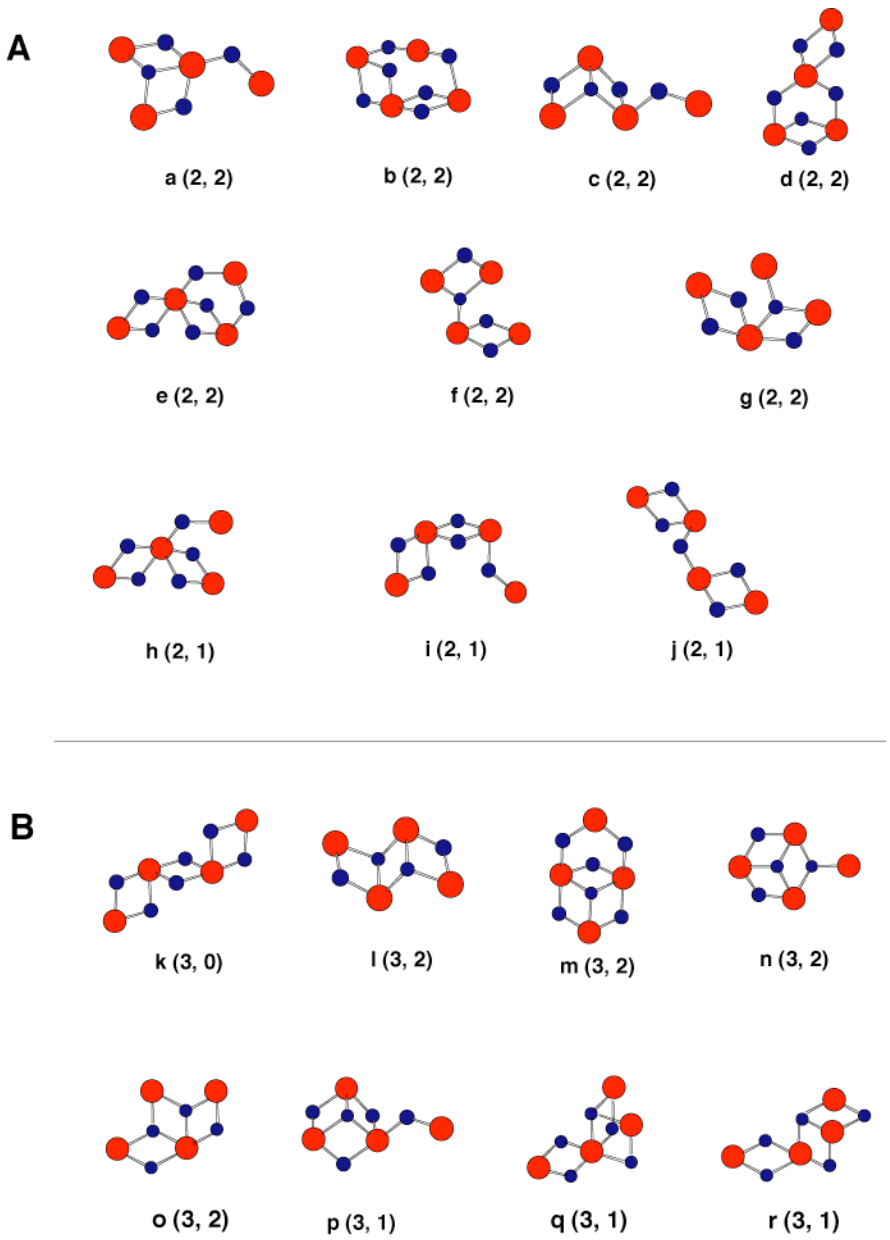
A
a (2, 2)
b (2, 2)
c (2, 2)
d (2, 2)
e (2, 2)
f (2, 2)
g (2, 2)
h (2, 1)
i (2, 1)
j (2, 1)
B
k (3, 0)
l (3, 2)
m (3, 2)
n (3, 2)
o (3, 2)
p (3, 1)
q (3, 1)
r (3, 1)

Fig. S1

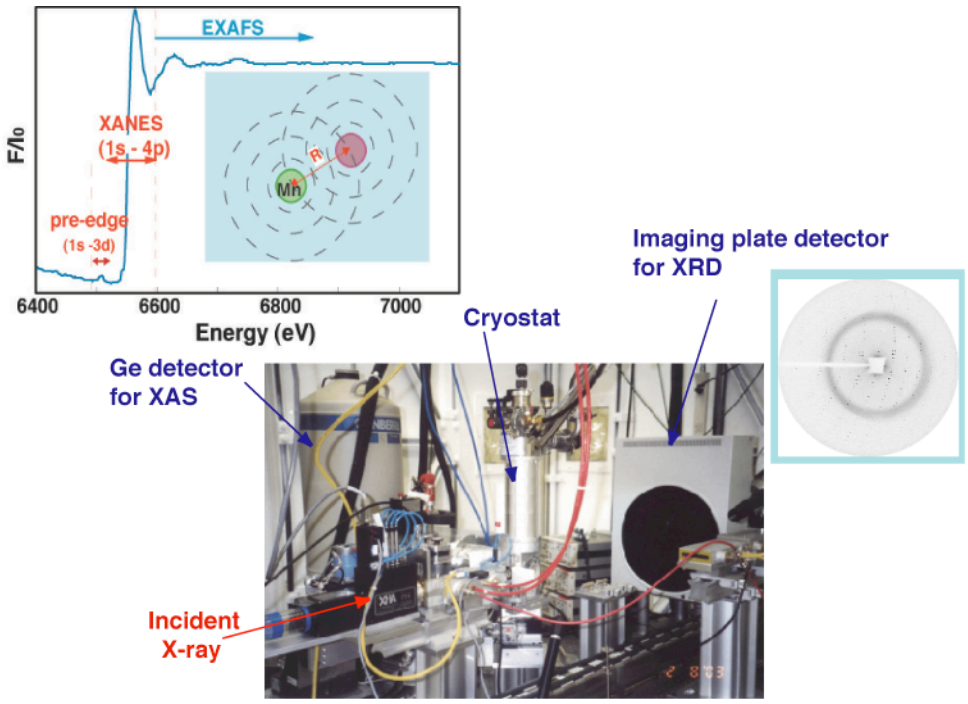
EXAFS
XANES
(1s - 4p)
pre-edge
(1s -3d)
F/Io
6400
6600
6800
7000
Energy (eV)
Mn
R
Imaging plate detector
for XRD
Cryostat
Ge detector
for XAS
Incident
X-ray

Fig. S2

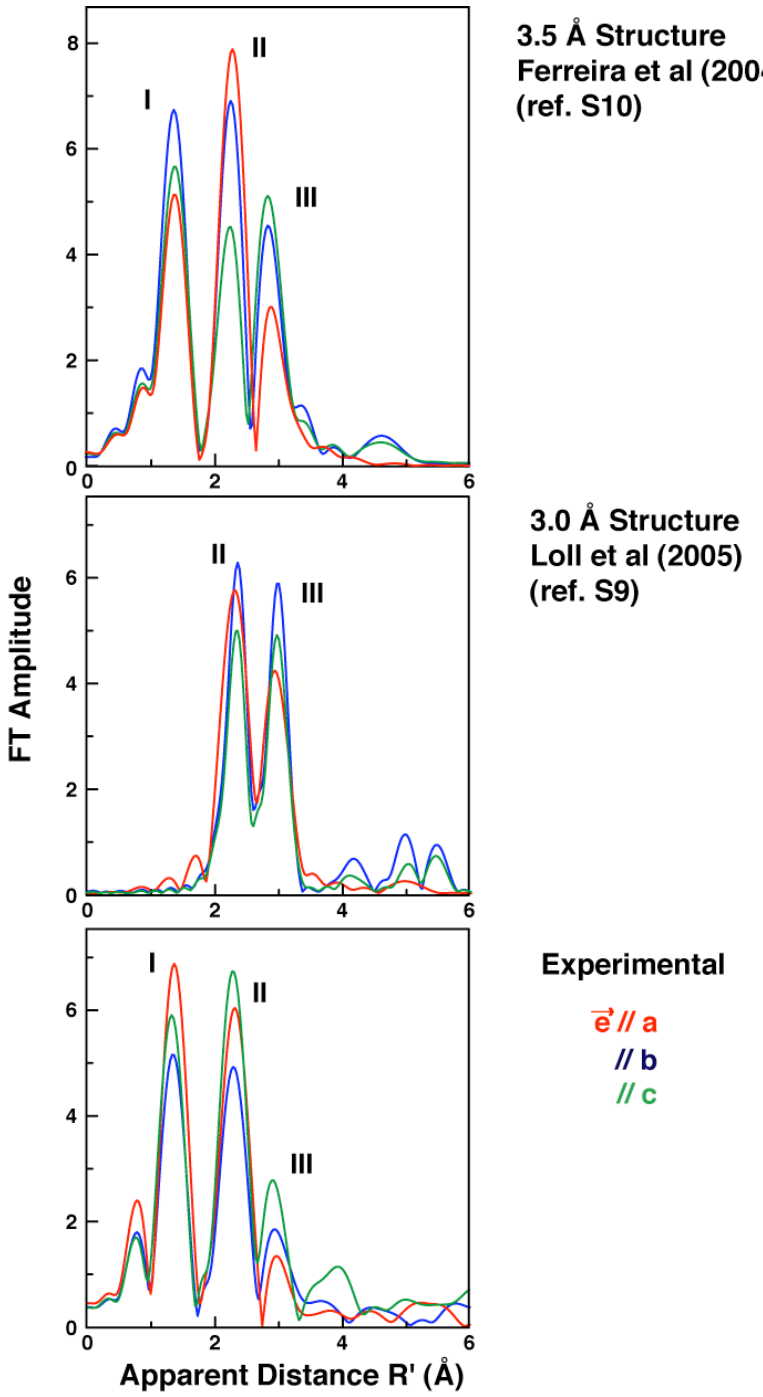
3.5 Å Structure
Ferreira et al (2004)
(ref. S10)
3.0 Å Structure
Loll et al (2005)
(ref. S9)
Experimental
e // a
// b
// c
I
II
III
FT Amplitude
Apparent Distance R' (Å)

Fig. S3

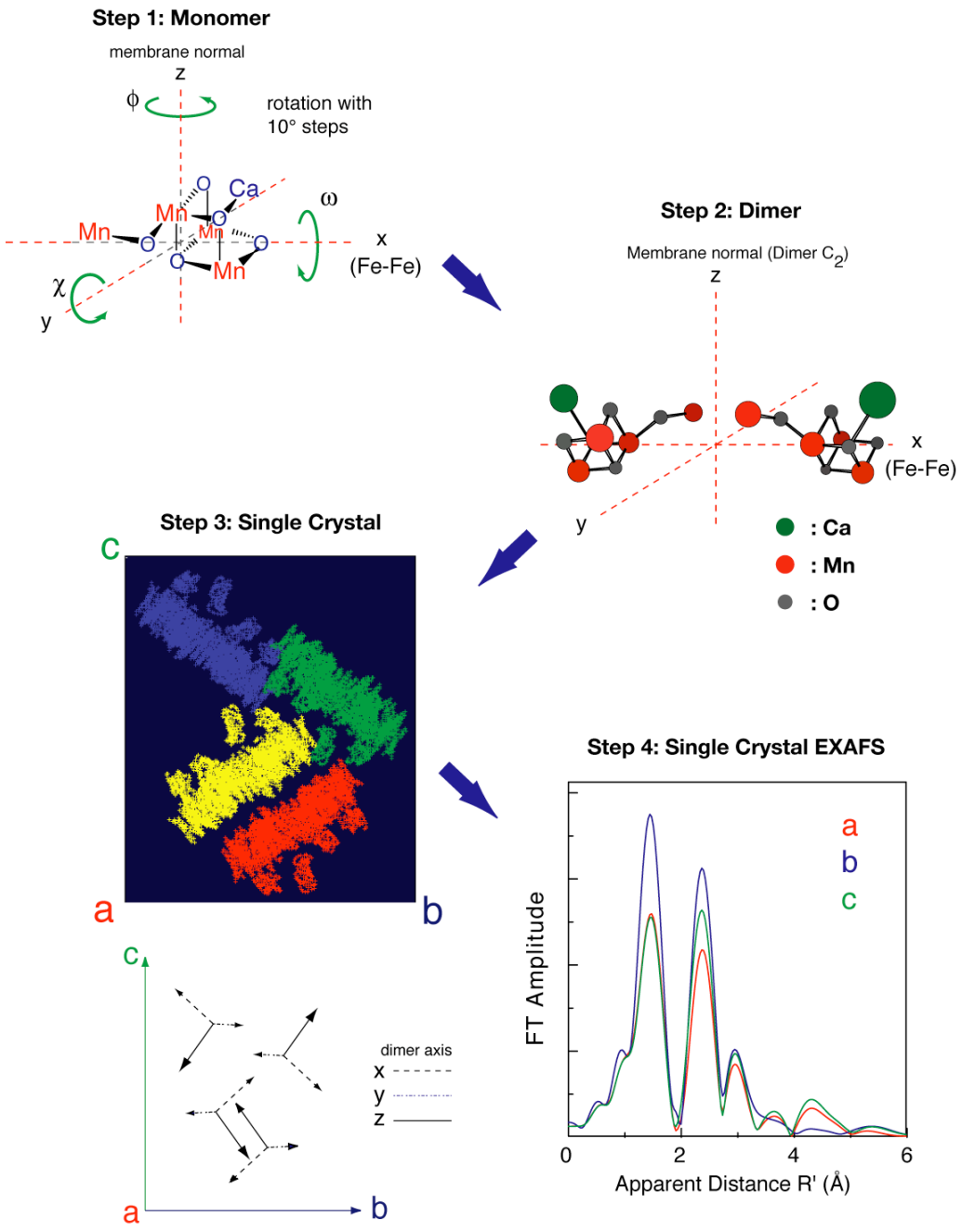
Step 1: Monomer
membrane normal
z
ϕ
rotation with
10° steps
Ca
Mn
Mn
Mn
Mn
ω
x
(Fe-Fe)
χ
y
Step 2: Dimer
Membrane normal (Dimer C2)
z
x
(Fe-Fe)
y
: Ca
: Mn
: O
Step 3: Single Crystal
c
a
b
c
a
b
dimer axis
x
y
z
Step 4: Single Crystal EXAFS
a
b
c
FT Amplitude
0
2
4
6
Apparent Distance R' (Å)

Fig. S4

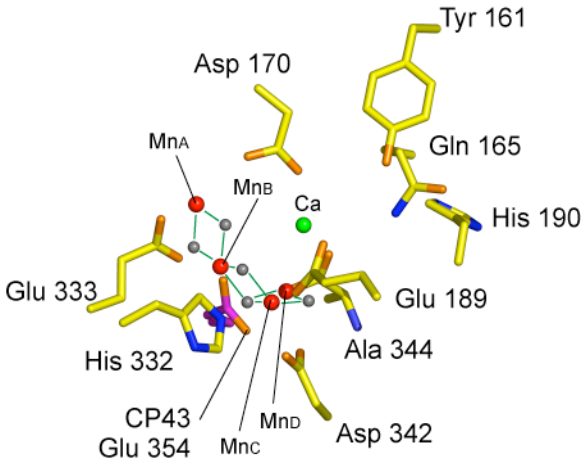
Tyr 161
Asp 170
Gln 165
MnA
MnB
Ca
His 190
Glu 333
Glu 189
Ala 344
His 332
CP43
Glu 354
MnC
MnD
Asp 342

Fig. S5

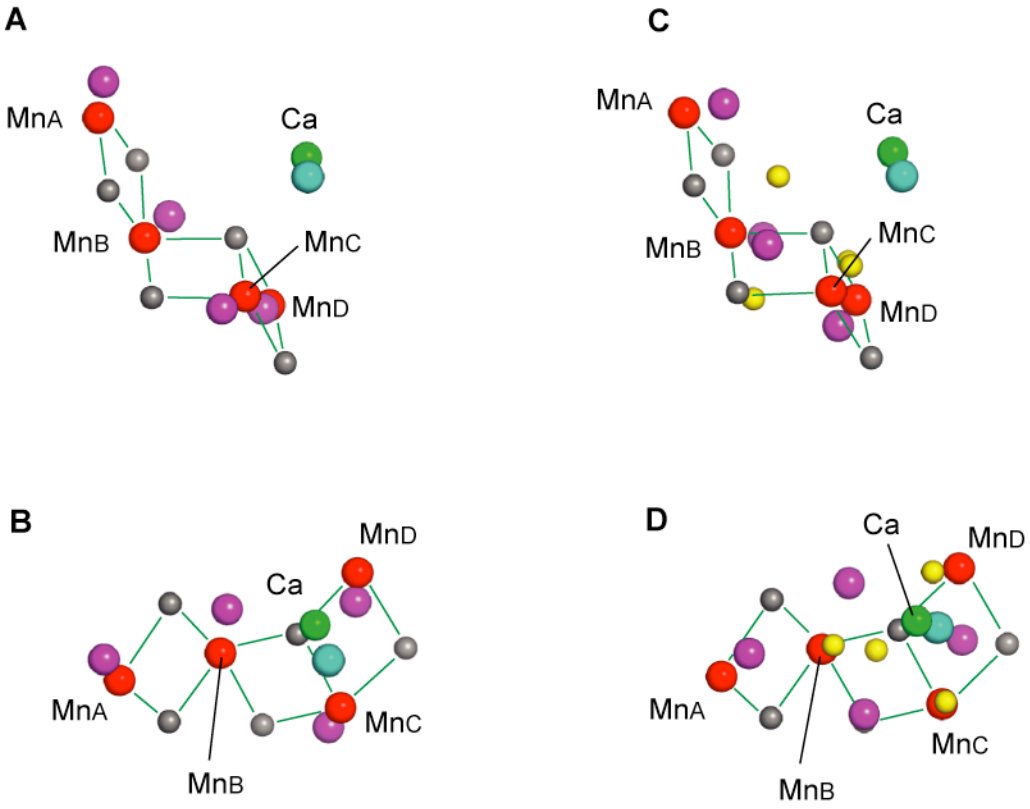
A
MnA
Ca
MnB
MnC
MnD
C
MnA
Ca
MnB
MnC
MnD
B
MnD
Ca
MnA
MnC
MnB
D
Ca
MnD
MnA
MnC
MnB

Fig. S6

Table S1. Mn EXAFS Curve-Fitting Parameters for PSII S_1 state in Solution and Single Crystals

Fourier peaks of the single crystal EXAFS spectra shown in Fig. 1B (single crystal) and 2B (solution) were fit using FEFF8 (*S5-8*). *R* is the distance from the absorbing atom Mn. *N* is the number of backscatterers from Mn. N_{iso} of 0.5 or 1.0 for the Mn-Mn shell translates into 1 or 2 Mn-Mn distances, while a N_{iso} of 0.5 for Mn-Ca shell translates into 2 Mn-Ca distances when the data are normalized on a per Mn basis (4Mn/PSII). N_{app} is proportional to $\cos^2\theta$, where θ is the angle between the X-ray **e**-field vector and the absorber-backscatterer vector. Debye-Waller factor, σ^2, was fixed to 0.002 ($Å^2*10^3$) for two interactions and 0.001 ($Å^2*10^3$) for one interaction based on the EXAFS fitting results of the previous PSII studies and model compounds (*S5, S6*). The numbers shown in bold type are the fixed parameters. Fit quality was evaluated using two different fit parameters, Φ, and ε^2 (*S5, S6*).

(A) Solution

	Fit#	Shell	*R* (Å)	N_{iso}	$\sigma^2(Å^2)*10^3$	$\Phi(*10^3)$	$\varepsilon^2(*10^5)$
Peak II	1-1	Mn-Mn	2.72	0.89	**0.002**	0.93	0.64
		Mn-Mn	2.81	0.45	**0.001**		
	1-2	Mn-Mn	2.72	0.64	**0.001**	1.48	1.02
		Mn-Mn	2.81	0.64	**0.001**		
Peak II + III	2-1	Mn-Mn	2.70	**1.0**	**0.002**	0.64	0.56
		Mn-Mn	2.79	**0.5**	**0.001**		
		Mn-Mn	3.25	**0.5**	**0.001**		
		Mn-Ca	3.41	**0.5**	**0.002**		
	2-2	Mn-Mn	2.72	**0.5**	**0.001**	0.93	0.71
		Mn-Mn	2.80	**0.5**	**0.001**		
		Mn-Mn	3.28	**0.5**	**0.001**		
		Mn-Ca	3.45	**0.5**	**0.002**		

(B) PSII Single Crystal

Axis		Fit#	Shell	R (Å)	N_{app}	σ^2(Å^2)*10^3	Φ(*10^3)	ε^2(*10^5)
a	Peak II	1-1	Mn-Mn	2.73	1.62	0.0030	0.45	0.53
		1-2	Mn-Mn	**2.72**	1.27	**0.002**	0.43	0.37
			Mn-Mn	**2.81**	0.33	**0.001**		
	Peak II + III	2-1	Mn-Mn	**2.72**	1.24	**0.002**	0.41	0.38
			Mn-Mn	**2.81**	0.44	**0.001**		
			Mn-Mn	**3.25**	0.20	**0.001**		
			Mn-Ca	**3.40**	0.29	**0.002**		

Axis		Fit#	Shell	R (Å)	N_{app}	σ^2(Å^2)*10^3	Φ(*10^3)	ε^2(*10^5)
b	Peak II	1-1	Mn-Mn	2.73	1.34	0.0037	0.48	0.61
		1-2	Mn-Mn	**2.72**	1.00	**0.002**	0.47	0.43
			Mn-Mn	**2.81**	0.23	**0.001**		
	Peak II + III	2-1	Mn-Mn	**2.72**	0.94	**0.002**	0.43	0.37
			Mn-Mn	**2.81**	0.38	**0.001**		
			Mn-Mn	**3.25**	0.46	**0.001**		
			Mn-Ca	**3.40**	0.48	**0.002**		

Axis		Fit#	Shell	R (Å)	N_{app}	σ^2(Å^2)*10^3	Φ(*10^3)	ε^2(*10^5)
c	Peak II	1-1	Mn-Mn	2.71	1.35	0.0016	0.29	0.35
		1-2	Mn-Mn	**2.72**	1.43	**0.002**	0.33	0.29
			Mn-Mn	**2.81**	0.00	**0.001**		
	Peak II + III	2-1	Mn-Mn	**2.72**	1.46	**0.002**	0.33	0.25
			Mn-Mn	**2.81**	0.12	**0.001**		
			Mn-Mn	**3.25**	0.28	**0.001**		
			Mn-Ca	**3.40**	0.93	**0.002**		

Table S2. Coordinates of Model II in the Context of the 3.0 Å XRD Structure (*S9*).

```
HEADER    ELECTRON TRANSPORT                      30-MAY-06
TITLE     STRUCTURE OF THE PHOTOSYNTHETIC MN4CA CLUSTER IN THE S1 STATE:
TITLE    2 PLACEMENT OF MODEL II WITHIN THE 3.0 Å STRUCTURE OF PSII
AUTHOR    J.YANO,J.KERN,K.SAUER,M.J.LATIMER,Y.PUSHKAR,J.BIESIADKA,
AUTHOR   2 B.LOLL,W.SAENGER,J.MESSINGER,A.ZOUNI,V.K.YACHANDRA
JRNL        AUTH   J.YANO,J.KERN,K.SAUER,M.J.LATIMER,Y.PUSHKAR,J.BIESIADKA,
JRNL        AUTH 2 B.LOLL,W.SAENGER,J.MESSINGER,A.ZOUNI,V.K.YACHANDRA
JRNL        TITL   WHERE WATER IS OXIDIZED TO DIOXYGEN: STRUCTURE OF
JRNL        TITL 2 THE PHOTOSYNTHETIC MN4CA CLUSTER
JRNL        REF    SCIENCE                         V. XXX  XXXX 2006
REMARK
REMARK     COORDINATES OF PROTEIN LIGANDS FROM D1 (PSBA, CHAIN A) AND CP43 (PSBC,
CHAIN C)
REMARK     ARE TAKEN FROM THE 3.0 Å RESOLUTION STRUCTURE OF PSII FROM
THERMOSYNECHOCOCCUS
REMARK     ELONGATUS(PDB-ID: 2AXT, LOLL ET AL, NATURE 438, 1040-1044 (2005)).
REMARK     THE STRUCTURE (MODEL II) AND  ORIENTATION OF THE OEC ARE OBTAINED
REMARK     FROM SIMULATION OF POLARISED EXAFS-SPECTRA, COLLECTED FROM PSII SINGLE
REMARK     CRYSTALS OF T. ELONGATUS IN THE S  STATE.
REMARK     POSITIONING OF THE OEC WITHIN THE LIGAND-ENVIRONMENT IS BASED
REMARK     UPON TRANSLATION OF THE EXAFS DERIVED MODEL INTO THE CENTER OF THE
REMARK     EXPERIMENTAL ELECTRON DENSITY ATTRIBUTED TO THE MN4CA CLUSTER, BEST FIT
REMARK     TO MN-ATOM POSITIONS FROM THE X-RAY STRUCTURE AND MINIMAL CONFLICTS
REMARK     WITH THE LIGAND ENVIRONMENT, FOR DETAILS SEE  YANO ET AL, SCIENCE (2006),
REMARK     AND SUPPORTING ONLINE MATERIAL.
REMARK
REMARK     THE LIGAND ASSIGNMENTS AND LIGAND-METAL DISTANCES MUST REMAIN
REMARK     TENTATIVE AT THIS POINT, BECAUSE MOVEMENT OF THE PROTEIN LIGAND RESIDUES
CAN
REMARK     RESULT FROM RADIATION DAMAGE TO THE METAL SITE DURING COLLECTION OF THE X-
RAY
REMARK     DIFFRACTION DATA (FOR DETAILS SEE YANO ET AL, SCIENCE (2006), AND YANO
REMARK     ET AL, PNAS 102, 12047-12052 (2005)). IN ADDITION THE LIGAND-COORDINATES
REMARK     OBTAINED FROM X-RAY DIFFRACTION WERE NOT SUBJECTED TO A NEW REFINEMENT OR
ENERGY
REMARK     MINIMIZATION AFTER PLACING OF THE EXAFS DERIVED METAL COORDINATES.
REMARK
REMARK     THE BRIDGING MOTIF TO CA IS NOT WELL DEFINED BY OUR EXPERIMENT.
REMARK
REMARK     GIVEN ARE THE COORDINATES FOR MONOMER I IN THE PSII DIMER.
REMARK     INCLUDED ARE THE RESIDUES IN THE DIRECT VICINITY
REMARK     OF THE OEC (T. ELONGATUS NUMBERING):
REMARK     D1 (PSBA):  ASP61, TYR161, GLN165, ASP170, GLU189, HIS190,
REMARK                 HIS332, GLU333, HIS337, ASP342, ALA344
REMARK     CP43 (PSBC): GLU354, ARG357
REMARK
REMARK     MN1 = "MN A" IN YANO ET AL, SCIENCE (2006)
REMARK     MN2 = "MN B" IN YANO ET AL, SCIENCE (2006)
REMARK     MN3 = "MN C" IN YANO ET AL, SCIENCE (2006)
REMARK     MN4 = "MN D" IN YANO ET AL, SCIENCE (2006)
REMARK
HETNAM     OEC OXYGEN EVOLVING SYSTEM
FORMUL     OEC    O5 CA1 MN4
CRYST1  127.692  225.403  306.106  90.00  90.00  90.00 P 21 21 21
ORIGX1      1.000000  0.000000  0.000000        0.00000
ORIGX2      0.000000  1.000000  0.000000        0.00000
```

```
ORIGX3      0.000000  0.000000  1.000000        0.00000
SCALE1      0.007831  0.000000  0.000000        0.00000
SCALE2      0.000000  0.004436  0.000000        0.00000
SCALE3      0.000000  0.000000  0.003267        0.00000
ATOM      1  N   ASP A  61      31.817  29.488  64.023  1.00 56.55
ATOM      2  CA  ASP A  61      31.697  30.053  65.353  1.00 57.98
ATOM      3  CB  ASP A  61      30.279  29.875  65.883  1.00 59.03
ATOM      4  CG  ASP A  61      29.243  30.577  65.015  1.00 61.78
ATOM      5  OD1 ASP A  61      29.529  31.695  64.531  1.00 62.12
ATOM      6  OD2 ASP A  61      28.137  30.020  64.809  1.00 62.77
ATOM      7  C   ASP A  61      32.711  29.296  66.161  1.00 59.72
ATOM      8  O   ASP A  61      33.430  28.494  65.598  1.00 60.71
ATOM      9  N   TYR A 161      36.360  45.377  60.328  1.00 52.45
ATOM     10  CA  TYR A 161      35.300  44.861  61.194  1.00 52.95
ATOM     11  CB  TYR A 161      34.099  44.369  60.381  1.00 54.12
ATOM     12  CG  TYR A 161      32.875  44.187  61.234  1.00 56.37
ATOM     13  CD1 TYR A 161      32.340  45.261  61.941  1.00 58.03
ATOM     14  CE1 TYR A 161      31.285  45.089  62.819  1.00 59.80
ATOM     15  CD2 TYR A 161      32.312  42.932  61.417  1.00 57.70
ATOM     16  CE2 TYR A 161      31.258  42.744  62.293  1.00 59.53
ATOM     17  CZ  TYR A 161      30.751  43.821  62.995  1.00 60.35
ATOM     18  OH  TYR A 161      29.737  43.615  63.902  1.00 61.31
ATOM     19  C   TYR A 161      35.772  43.757  62.105  1.00 51.61
ATOM     20  O   TYR A 161      35.328  43.654  63.244  1.00 53.36
ATOM     21  N   GLN A 165      35.950  43.566  66.283  1.00 49.73
ATOM     22  CA  GLN A 165      35.243  42.534  67.007  1.00 51.85
ATOM     23  CB  GLN A 165      34.204  41.907  66.082  1.00 52.68
ATOM     24  CG  GLN A 165      33.173  42.900  65.588  1.00 53.01
ATOM     25  CD  GLN A 165      32.377  43.491  66.728  1.00 52.91
ATOM     26  OE1 GLN A 165      32.180  44.707  66.799  1.00 50.57
ATOM     27  NE2 GLN A 165      31.913  42.628  67.637  1.00 52.38
ATOM     28  C   GLN A 165      36.139  41.459  67.622  1.00 53.17
ATOM     29  O   GLN A 165      35.692  40.675  68.448  1.00 54.30
ATOM     30  N   ASP A 170      33.949  36.700  62.485  1.00 55.22
ATOM     31  CA  ASP A 170      32.960  37.724  62.187  1.00 57.18
ATOM     32  CB  ASP A 170      32.870  38.766  63.307  1.00 58.77
ATOM     33  CG  ASP A 170      32.107  38.249  64.523  1.00 63.13
ATOM     34  OD1 ASP A 170      31.363  37.241  64.351  1.00 65.39
ATOM     35  OD2 ASP A 170      32.225  38.836  65.640  1.00 62.19
ATOM     36  C   ASP A 170      33.539  38.348  60.940  1.00 57.44
ATOM     37  O   ASP A 170      34.689  38.086  60.614  1.00 57.76
ATOM     38  N   GLU A 189      22.815  43.835  65.638  1.00 55.95
ATOM     39  CA  GLU A 189      23.884  44.168  66.565  1.00 56.43
ATOM     40  CB  GLU A 189      25.119  43.289  66.306  1.00 59.17
ATOM     41  CG  GLU A 189      24.850  41.764  66.407  1.00 64.04
ATOM     42  CD  GLU A 189      26.104  40.910  66.687  1.00 65.98
ATOM     43  OE1 GLU A 189      27.159  41.162  66.048  1.00 67.53
ATOM     44  OE2 GLU A 189      26.020  39.974  67.533  1.00 65.76
ATOM     45  C   GLU A 189      24.292  45.623  66.581  1.00 54.99
ATOM     46  O   GLU A 189      24.834  46.089  67.568  1.00 54.83
ATOM     47  N   HIS A 190      24.019  46.344  65.501  1.00 53.16
ATOM     48  CA  HIS A 190      24.390  47.754  65.409  1.00 52.20
ATOM     49  CB  HIS A 190      25.566  47.900  64.452  1.00 53.32
ATOM     50  CG  HIS A 190      26.792  47.144  64.869  1.00 54.34
ATOM     51  CD2 HIS A 190      27.307  45.969  64.435  1.00 53.85
ATOM     52  ND1 HIS A 190      27.655  47.604  65.838  1.00 54.21
ATOM     53  CE1 HIS A 190      28.648  46.746  65.982  1.00 54.34
ATOM     54  NE2 HIS A 190      28.461  45.746  65.143  1.00 53.03
ATOM     55  C   HIS A 190      23.275  48.696  64.960  1.00 51.15
ATOM     56  O   HIS A 190      23.450  49.908  64.930  1.00 50.81
ATOM     57  N   HIS A 332      20.248  34.370  66.477  1.00 46.62
```

```
ATOM     58  CA  HIS A 332      21.543  34.236  65.824  1.00 45.81
ATOM     59  CB  HIS A 332      22.084  35.582  65.386  1.00 47.31
ATOM     60  CG  HIS A 332      22.902  36.258  66.425  1.00 48.42
ATOM     61  CD2 HIS A 332      24.206  36.617  66.439  1.00 50.11
ATOM     62  ND1 HIS A 332      22.383  36.644  67.635  1.00 49.81
ATOM     63  CE1 HIS A 332      23.334  37.218  68.351  1.00 52.92
ATOM     64  NE2 HIS A 332      24.451  37.215  67.648  1.00 51.41
ATOM     65  C   HIS A 332      22.550  33.564  66.699  1.00 45.18
ATOM     66  O   HIS A 332      22.644  33.853  67.874  1.00 43.62
ATOM     67  N   GLU A 333      23.312  32.665  66.100  1.00 45.05
ATOM     68  CA  GLU A 333      24.318  31.916  66.813  1.00 45.00
ATOM     69  CB  GLU A 333      25.504  32.825  67.098  1.00 45.38
ATOM     70  CG  GLU A 333      26.510  32.823  65.953  1.00 46.79
ATOM     71  CD  GLU A 333      27.216  34.144  65.753  1.00 48.97
ATOM     72  OE1 GLU A 333      27.749  34.726  66.733  1.00 47.95
ATOM     73  OE2 GLU A 333      27.243  34.593  64.586  1.00 50.51
ATOM     74  C   GLU A 333      23.736  31.291  68.082  1.00 45.29
ATOM     75  O   GLU A 333      24.273  31.413  69.184  1.00 46.22
ATOM     76  N   HIS A 337      26.274  31.145  72.879  1.00 50.11
ATOM     77  CA  HIS A 337      26.239  32.003  74.060  1.00 50.49
ATOM     78  CB  HIS A 337      25.169  33.082  73.888  1.00 51.08
ATOM     79  CG  HIS A 337      25.392  33.962  72.702  1.00 51.90
ATOM     80  CD2 HIS A 337      26.103  35.102  72.558  1.00 52.14
ATOM     81  ND1 HIS A 337      24.911  33.651  71.453  1.00 53.83
ATOM     82  CE1 HIS A 337      25.319  34.562  70.587  1.00 54.84
ATOM     83  NE2 HIS A 337      26.045  35.452  71.232  1.00 54.10
ATOM     84  C   HIS A 337      26.050  31.325  75.417  1.00 51.02
ATOM     85  O   HIS A 337      25.216  30.434  75.563  1.00 51.26
ATOM     86  N   ASP A 342      25.767  40.170  74.895  1.00 58.66
ATOM     87  CA  ASP A 342      26.515  39.847  73.693  1.00 60.29
ATOM     88  CB  ASP A 342      25.577  39.871  72.478  1.00 60.43
ATOM     89  CG  ASP A 342      26.216  39.287  71.210  1.00 63.40
ATOM     90  OD1 ASP A 342      27.427  38.988  71.227  1.00 64.19
ATOM     91  OD2 ASP A 342      25.513  39.123  70.179  1.00 63.77
ATOM     92  C   ASP A 342      27.630  40.873  73.519  1.00 62.29
ATOM     93  O   ASP A 342      27.470  41.837  72.787  1.00 63.48
ATOM     94  N   ALA A 344      30.591  40.388  72.076  1.00 71.12
ATOM     95  CA  ALA A 344      31.525  39.798  71.108  1.00 71.83
ATOM     96  CB  ALA A 344      32.398  38.734  71.818  1.00 71.85
ATOM     97  C   ALA A 344      30.811  39.189  69.873  1.00 72.39
ATOM     98  O   ALA A 344      30.820  39.825  68.780  1.00 73.77
ATOM     99  OXT ALA A 344      30.216  38.092  69.986  1.00 72.94
ATOM    100  N   GLU C 354      31.858  32.951  73.818  1.00 61.10
ATOM    101  CA  GLU C 354      32.400  33.650  72.659  1.00 60.53
ATOM    102  CB  GLU C 354      31.453  34.757  72.158  1.00 60.73
ATOM    103  CG  GLU C 354      30.433  34.301  71.108  1.00 62.54
ATOM    104  CD  GLU C 354      29.730  35.457  70.401  1.00 63.89
ATOM    105  OE1 GLU C 354      29.103  36.278  71.098  1.00 65.12
ATOM    106  OE2 GLU C 354      29.798  35.555  69.149  1.00 64.62
ATOM    107  C   GLU C 354      33.723  34.258  73.045  1.00 60.04
ATOM    108  O   GLU C 354      34.561  34.536  72.201  1.00 59.19
ATOM    109  N   ARG C 357      37.711  34.032  71.998  1.00 55.60
ATOM    110  CA  ARG C 357      38.472  34.821  71.051  1.00 55.11
ATOM    111  CB  ARG C 357      37.528  35.553  70.115  1.00 53.33
ATOM    112  CG  ARG C 357      36.687  36.573  70.842  1.00 53.20
ATOM    113  CD  ARG C 357      35.904  37.426  69.903  1.00 51.24
ATOM    114  NE  ARG C 357      35.008  36.635  69.096  1.00 49.28
ATOM    115  CZ  ARG C 357      34.136  37.159  68.259  1.00 51.48
ATOM    116  NH1 ARG C 357      34.062  38.461  68.144  1.00 53.46
ATOM    117  NH2 ARG C 357      33.352  36.393  67.530  1.00 52.97
ATOM    118  C   ARG C 357      39.347  35.854  71.737  1.00 56.50
```

```
ATOM    119  O   ARG C 357      40.327  36.319  71.172  1.00 58.62
HETATM  120 CA1  OEC    55      29.865  39.505  66.847  1.00 65.62
HETATM  121 MN1  OEC    55      28.652  35.878  64.653  1.00 65.62
HETATM  122 MN2  OEC    55      28.000  36.319  67.248  1.00 65.62
HETATM  123 MN3  OEC    55      26.844  38.606  68.151  1.00 65.62
HETATM  124 MN4  OEC    55      29.045  38.042  69.811  1.00 65.62
HETATM  125  O1  OEC    55      28.626  37.993  67.846  1.00 65.62
HETATM  126  O2  OEC    55      29.596  35.970  66.356  1.00 65.62
HETATM  127  O3  OEC    55      27.262  38.795  70.113  1.00 65.62
HETATM  128  O4  OEC    55      27.248  36.227  65.549  1.00 65.62
HETATM  129  O5  OEC    55      26.225  36.878  67.577  1.00 65.62
END
```

Supplementary Material References

S1. J. Kern, *et al*., *Biochim. Biophys. Acta* **1706**, 147 (2005).

S2. J. Yano, *et al*., *Proc. Natl. Acad. Sci. USA* **102**, 12047 (2005).

S3. Z. Otwinowski, W. Minor, *Methods Enzymol*. **276**, 307-326 (1997).

S4. A. G. W. Leslie, *Joint CCP4+ESF-EAMCB Newsletter on Protein Crystallography*, No. 26, (1992).

S5. J. H. Robblee, *et al*., *J. Am. Chem. Soc*. **124**, 7459 (2002).

S6. R. M. Cinco et al, *et al*., *Inorg. Chem*. **38**, 5988 (1999).

S7. J. J. Rehr, R. C. Albers, *Rev. Mod. Phys*. **72**, 621, (2000).

S8. M. J. Newville, *Synchrotron Rad*. 8, 322, (2001).

S9. B. Loll, J. Kern, W. Saenger, A. Zouni, J. Biesiadka, *Nature*, **438**, 1040. (2005).

S10. K. N. Ferreira, T. M. Iverson, K. Maghlaoui, J. Barber, S. Iwata, *Science* **303**, 1831 (2004).

S11. J. Yano, *et al*., *J. Am. Chem. Soc*. **127**, 14974 (2005).